



Synthesis and highly efficient photocatalytic activity of mixed oxides derived from ZnNiAl layered double hydroxides

Li ZHANG¹, Chao-hua DAI¹, Xiu-xiu ZHANG³, You-nian LIU², Jian-hui YAN^{1,2,3}

1. College of Chemistry and Chemical Engineering,

Hunan Institute of Science and Technology, Yueyang 414006, China;

2. School of Chemistry and Chemical Engineering, Central South University, Changsha 410083, China;

3. College of Chemical Engineering, Xiangtan University, Xiangtan 411105, China

Received 21 September 2015; accepted 13 January 2016

Abstract: ZnO/NiO/ZnAl₂O₄ mixed-metal oxides were successfully synthesized through a hydrotalcite-like precursor route, in which appropriate amounts of metal salts solutions were mixed to obtain a new series of ZnNiAl layered double hydroxides (LDHs) as precursors, followed by calcination under different temperatures. The as-obtained samples were characterized by SEM, HRTEM, TEM, XRD, BET, TG-DTA, and UV-Vis spectra techniques. The photocatalytic activities of the samples were evaluated by degradation of methyl orange (MO) under the simulated sunlight irradiation. The effects of Zn/Ni/Al mole ratio and calcination temperature on the composition, morphology and photocatalytic activity of the samples were investigated in detail. The results indicated that compared with ZnNiAl-LDHs, the mixed-metal oxide showed superior photocatalytic performance for the degradation of MO. A maximum of 97.3% photocatalytic decoloration rate within 60 min was achieved from the LDH with the Zn/Ni/Al mole ratio of 2:1:1 and the calcination temperature of 500 °C, which much exceeded that of Degussa P25 under the same conditions. The possible mechanism of photocatalytic degradation over ZnO/NiO/ZnAl₂O₄ was discussed.

Key words: ZnNiAl layered double hydroxide; mixed oxide; photocatalytic degradation; photocatalytic activity

1 Introduction

For environmental remediation and pollution control, the effective removal of cationic dyes from the textile industry has always been a challenging issue. With the rapid development of nanostructured semiconductors for efficient harvesting abundant solar light, photocatalysis has received extensive attention for the removal of organic dyestuffs [1,2]. In particular, the mixed metal oxides prepared by thermal treatment of layered double hydroxides (LDHs), acted as photocatalysts, have been the focus of attention due to their versatility of chemical composition and high dispersion [3–5]. Different metals and proportion in LDHs can be controlled, which could tune the semiconductor properties of the layered-structure LDH materials and facilitate the transfer of the photogenerated electrons to the surface of photocatalysts, and this might

provide great potential for their application in dye degradation [6,7]. ZHAO et al [8] have recently conducted studies on the thermal treatment of ZnAl-LDH at 800 °C with different Zn²⁺/Al³⁺ mole ratios, which showed an enhanced photocatalytic activity with an increase in the mole ratio. CARRIAZO et al [9] also reported that the photocatalytic activity and crystallinity of the metal oxide produced from Zn–Al–CO₃–LDH are improved with proper control of calcination temperature and Zn²⁺/Al³⁺ mole ratio. Furthermore, there are reports on the introduction of In [10,11] and Ce [12] integrated on LDH materials as efficient photocatalysts. However, to the best of our knowledge, the use of earth-abundant metals such as Ni and Cu for the generation of LDH precursors is rare, especially for the degradation of MO. It is of great significance to employ the cheap metals for the synthesis of high-performance photocatalysts. On the other hand, although it is known that the replacement of M²⁺ by a higher-valance metal ion of similar radius is

Foundation item: Project (21306041) supported by the National Natural Science Young Foundation of China; Project (21271071) supported by the National Natural Science Foundation of China; Project (15A076) supported by the Scientific Research Foundation of Hunan Provincial Education Department of China

Corresponding author: Jian-hui YAN; Tel: +86-730-8640436; E-mail: yanjh58@163.com

DOI: 10.1016/S1003-6326(16)64360-1

beneficial for the improvement of photocatalytic properties of LDHs [13–15], it has been scarcely reported about the partial substitution of M^{2+} by another type of M^{2+} .

In this work, we synthesized a series of ZnO/NiO/ZnAl₂O₄ mixed-metal oxides with large specific area and studied their physicochemical properties. Especially, the incorporation of Ni²⁺ cation contributes to the enhanced photocatalytic activities for the degradation of high-concentration MO compared with ZnAl-LDHs under simulated sunlight irradiation. Besides providing new highly efficient sun-light-induced photocatalysts, the present work has further implications to photocatalytic degradation of organic pollutants.

2 Experimental

2.1 Synthesis of precursor

We followed the synthetic procedure described by ZHAO et al [8]. Typically, keeping the total concentration of metal ions fixed at 1.0 mol/L, Zn(NO₃)₂·6H₂O, Ni(NO₃)₂·6H₂O and Al(NO₃)₃·9H₂O with different Zn²⁺/Ni²⁺/Al³⁺ mole ratios were dissolved in deionized water to form a clear solution at room temperature. NaOH and Na₂CO₃ were mixed in deionized water to form an alkali solution ($[OH^-]=1.6[Zn^{2+}]+[Ni^{2+}]+[Al^{3+}]$ and $[CO_3^{2-}]=2.0[Al^{3+}]$), which was subsequently added drop-wise into the above salt solution under vigorous stirring at room temperature. The pH value of the solution was adjusted to 8–9. The mixture was transferred into a teflon-lined autoclave and thermally treated at 150 °C for 10 h, and then filtered and washed with distilled water until pH=7. The solid was oven-dried at 60 °C overnight to obtain ZnNiAl-LDHs precursors with different Zn²⁺/Ni²⁺/Al³⁺ mole ratios (i.e., 1:1:1, 2:1:1, 3:1:1, 1:2:1, 1:3:1, 2:1:1, 3:1:1). The one with Zn²⁺/Ni²⁺/Al³⁺ mole ratio of 2:1:1 is specifically denoted herein as ZNA-2-LDH.

2.2 Synthesis of mixed-metal oxides

The precursors were calcined in air at 400, 500, 600, 700, and 800 °C for 4 h, respectively, and allowed to cool down to room temperature. These obtained mixed-metal oxides with the Zn/Ni/Al mole ratio of 2:1:1 were denoted as ZNA-2-400, ZNA-2-500, ZNA-2-600, ZNA-2-700 and ZNA-2-800, respectively, where the first number refers to the mole ratio of Zn²⁺/Ni²⁺/Al³⁺ and the second number refers to the calcination temperature. In comparison, the ZnAl-LDH with mole ratio of Zn²⁺/Al³⁺ being 3:1 was prepared in the similar way without Ni addition.

2.3 Characterization

The crystal phase and size of samples were

identified by powder X-ray diffraction (XRD, Bruker D8) using Cu K_α radiation ($\lambda=1.5418 \text{ \AA}$) at a scan speed of 0.05 (°)/s, a voltage of 40 kV, and a current of 300 mA. The surface morphologies of samples were observed by scanning electron microscopy (SEM, Nova Nano 230) operated at 30 kV and transmission electron microscopy (TEM, JEOL JEM-2010) operated at 200 kV. UV-Vis diffused reflectance spectra (DRS) of the samples were obtained using a UV-Vis spectro photometer (UV-2550, Shimadzu, Japan). Brunauer-Emmett-Teller (BET) surface areas were determined over the nitrogen adsorption isotherms apparatus (ST-08 analyzer), and all samples were degassed at 200 °C overnight before measurements.

2.4 Photocatalytic activity evaluation

The photocatalytic activity of the samples was evaluated by degradation of MO (100 mg/L solution). A 150 W xenon lamp with $\lambda=200-900 \text{ nm}$ was used as the simulated sunlight source. For each run, 0.3 g of catalyst was added into 600 mL MO solution and stirred for 30 min in the dark to establish an adsorption/desorption equilibrium. Then, the solution was exposed to simulated sunlight for photocatalytic reaction. The luminous intensity was measured at 100 mW/m² by the auto-range ST-85 optical radiometer (Photoelectric Instrument Factory of Beijing Normal University, China). During irradiation, the catalyst was kept in suspension state by a magnetic stirrer. Samples for analysis were extracted through pipette every 10 min and centrifuged immediately. Using a 752 UV-Vis spectrophotometer at the maximum absorption wavelength of $\lambda_{\text{max}}=465 \text{ nm}$ of MO, the absorbance of the suspension and initial solution was determined, respectively. Decoloration rates are presented as c/c_0 , where c_0 and c are the initial concentration of MO at adsorption/desorption equilibrium and the concentration of MO at a specified irradiation time, respectively. Blank experiments, i.e., without catalyst or in the dark, were carried out under the same condition. Each set of measurements was repeated three times, and the experimental error was within $\pm 5\%$.

3 Results and discussion

3.1 Characterization

As shown in Fig. 1, almost the same typical structures are observed in the XRD patterns of ZnAl-LDH ($n(\text{Zn}^{2+})/n(\text{Al}^{3+})=3:1$) and ZnNiAl-LDH ($n(\text{Zn}^{2+})/n(\text{Ni}^{2+})/n(\text{Al}^{3+})=2:1:1$) precursors. The diffraction peaks at $2\theta=11.7^\circ$, 23.5° , 34.6° , 39.2° , 46.7° , 52.9° , 56.3° , 60.2° and 61.5° can be assigned to (003), (006), (009), (015), (018), (1010), (0111), (110) and (113) reflections of LDH, respectively, characteristic of a layered structure [16,17]. Besides, the reflections at $2\theta=32^\circ$ and

37° can be indexed to $\text{Zn}(\text{OH})_2$ (JCPDS 48–1066). In other words, there is the co-existence of $\text{Zn}(\text{OH})_2$ and LDHs. No diffraction peaks corresponding to nickel compounds are observed, suggesting that the Ni^{2+} ions are well dispersed into the ZnAl-LDH lattice. Moreover, the ZnNiAl-LDH becomes dominant compared with the ZnAl-LDH, resulting in a well-crystalline product. It is plausible that the incorporation of Ni^{2+} results in strong electrostatic interaction between the host layer and guest carbonate and hence improved crystallinity [11].

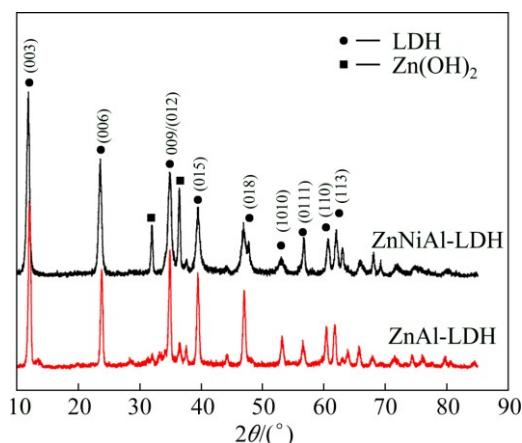


Fig. 1 XRD patterns of ZnAl-LDH and ZnNiAl-LDH

Figure 2 indicates the XRD patterns of ZnNiAl-LDH calcined at different temperatures (400–800 °C). The reflections corresponding to LDHs completely disappear and new reflections appear after calcination. The peaks become sharp with increasing calcination temperature. The reflections at $2\theta=31.8^\circ$, 34.4° , 36.2° , 47.6° , 56.6° , and 62.9° can be indexed to hexagonal Wurtzite structure ZnO (JCPDS No. 36–1451), whereas those at $2\theta=43.3^\circ$, 62.8° and 36.9° can be indexed to NiO (JCPDS No. 47–1049) and ZnAl_2O_4 (JCPDS No. 05–0669), respectively. The ZnAl_2O_4 spinel occurs at above 500 °C, in agreement with the works of AHMED et al [18] and ZOU et al [19]. The results may be ascribed to the homogeneous distribution of metal ions inside ZnNiAl-LDH, which facilitates the formation of well-dispersed and crystalline mixed metal oxides through a topotactic process upon calcinations [20]. There is no detection of signals corresponding to Al_2O_3 phase, implying that Al_2O_3 is amorphous. This is because with the collapse of ZnNiAl-LDH layered structure upon calcination, there is the generation of ZnO and Al_2O_3 that subsequently give rise to the formation of spinel ZnAl_2O_4 [20]. It is worth pointing out that the amorphous Al_2O_3 as a dispersant is capable of inhibiting the aggregation of ZnO and NiO particles.

From the XRD patterns of ZnAl-LDH ($n(\text{Zn}^{2+})/n(\text{Al}^{3+})=3:1$) and ZnNiAl-LDH (variable ratio) precursors calcined at 500 °C (Fig. 3), it is obvious that

the thermal treatment leads to the collapse of the lamellar structure, and new diffraction lines ascribed to different metal oxides, ZnO (JCPDS No. 36–1451), NiO (JCPDS No. 47–1049) and a little ZnAl_2O_4 (JCPDS No. 05–0669) phase. With increase of Zn^{2+} content, the intensities of diffraction peaks of mixed metal oxides gradually increase. The peaks of ZNA-2-500 are most intense among the samples, suggesting a well-crystalline structure. The samples with $\text{Zn}^{2+}/\text{Ni}^{2+}/\text{Al}^{3+}$ mole ratios of 1:1:1, 1:1:2, and 1:1:3 (i.e., decrease in Zn^{2+} content) exhibit no significant difference in the XRD patterns, and all the patterns display a feature of broad reflections, characteristic of poorly-crystalline structure, which may result in relatively low photocatalytic activity. On the other hand, the peak intensities of samples are found to be enhanced with the increase of Ni^{2+} content ($\text{Zn}^{2+}/\text{Ni}^{2+}/\text{Al}^{3+}$ mole ratios of 1:1:1, 1:2:1 and 1:3:1).

Four stages of mass losses are observed in the TG-DTA curves (Fig. 4) of ZNA-2-LDH. The first stage of mass loss (25–200 °C) corresponds to the removal of physically adsorbed and interlayer water molecules. The

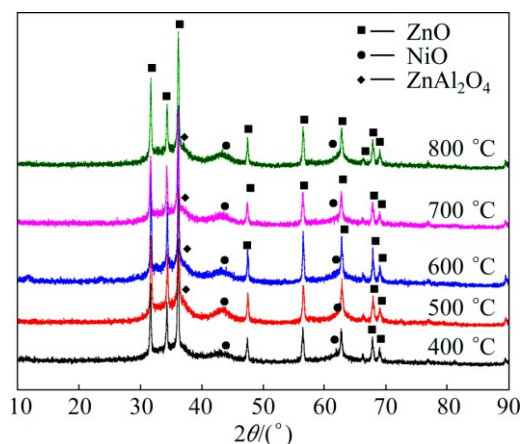


Fig. 2 XRD patterns of ZnNiAl-LDH calcined at different temperatures

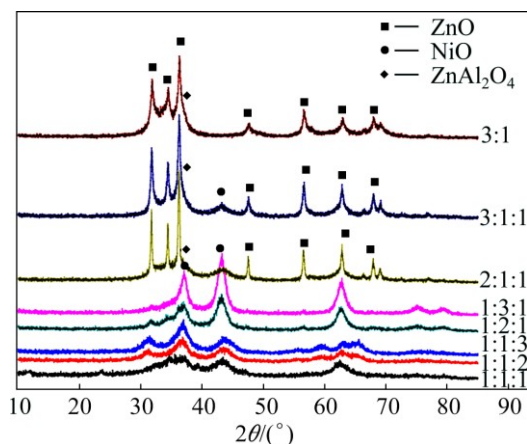


Fig. 3 XRD patterns of ZnAl-LDH with mole ratio of Zn/Al being 3:1 and ZnNiAl-LDHs with different Zn/Ni/Al mole ratios

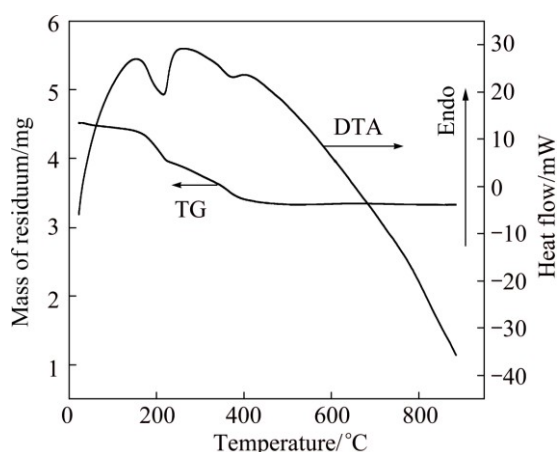


Fig. 4 TG-DTA curves of ZNA-2-LDH

second one that occurs in the 200–260 °C range is ascribed to loss of hydroxyl groups from the brucite-like layer, meanwhile the corresponding endothermic peak is observed at 245 °C. The third one (260–450 °C) can be ascribed to the elimination of interlayer carbonate anions with the destruction of layered structure [21,22]. The fourth mass loss beyond 450 °C is attributed to the loss of oxygen and CO₂ through slow decomposition of Zn/Ni/Al oxycarbonate which is likely to exist after the

decomposition of LDH-like structures [15]. The overall behaviors of ZNA-2-LDH are largely in agreement with that reported for ZnAl-LDH by KOILRAJ et al [23].

The SEM images of ZNA-2-LDH before and after calcination are presented in Fig. 5. It can be seen that the ZNA-2-LDH before calcination is made up of agglomerated platelet-like particles, and the platelets have a side length of 20–50 nm (Fig. 5(a)). After calcination at 400 °C, there is the collapse of LDH structure and the platelets become irregular aggregates (Fig. 5(b)). With calcination temperature increase to 500–600 °C, the morphology of the nanoparticles becomes spherical, about 20 nm in diameter (Figs. 5(c) and (d)), which would provide abundant adsorption sites for adsorbate.

The TEM and HRTEM images of ZNA-2-LDH and ZNA-2-500 are presented in Fig. 6. There is uniform distribution of LDH particles (dark and bright fields in Figs. 6(a) and (b)) in ZNA-2-LDH, some in the form of irregular hexagon. In Fig. 6(c), the average particle size of ZNA-2-LDH decreases upon calcination at 500 °C to the formation of ZNA-2-500. The HRTEM image and EDX pattern of ZNA-2-500 are presented in Figs. 6(d) and (e), respectively. The former reveals that the heterojunction structures form between ZnO, NiO and

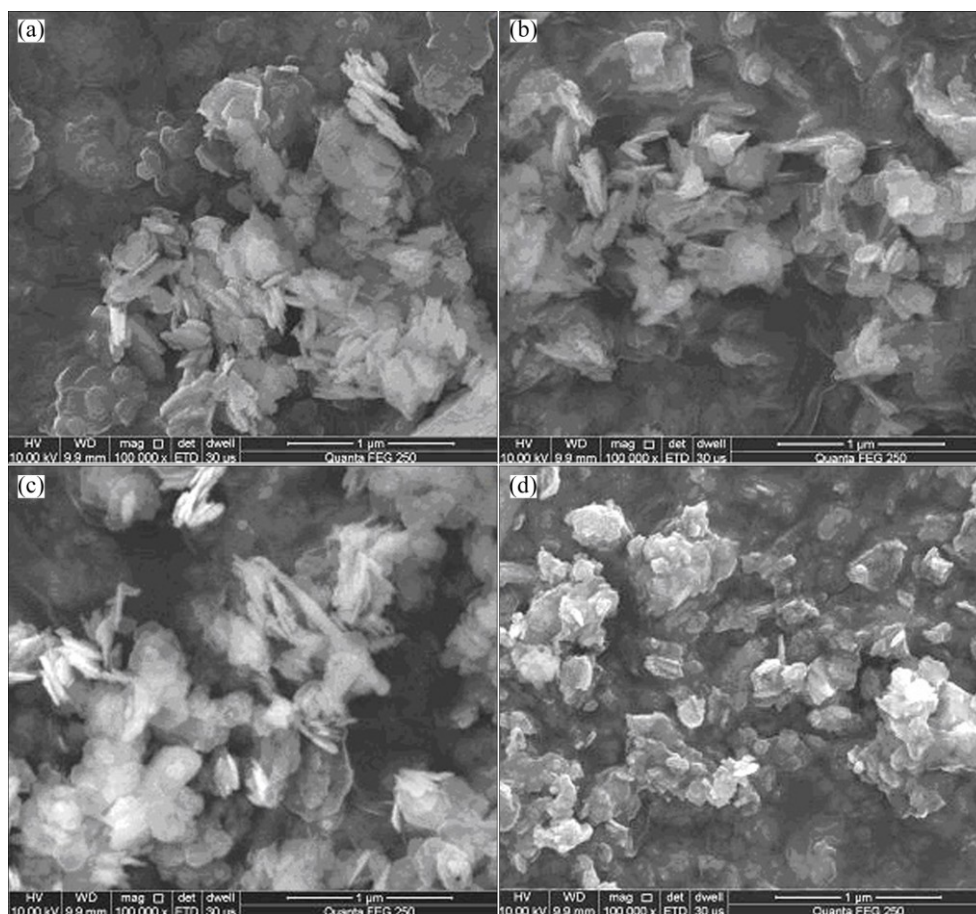


Fig. 5 SEM images of ZNA-2-LDH (a) and ZNA-2-LDH calcined at 400 °C (b), 500 °C (c) and 600 °C (d)

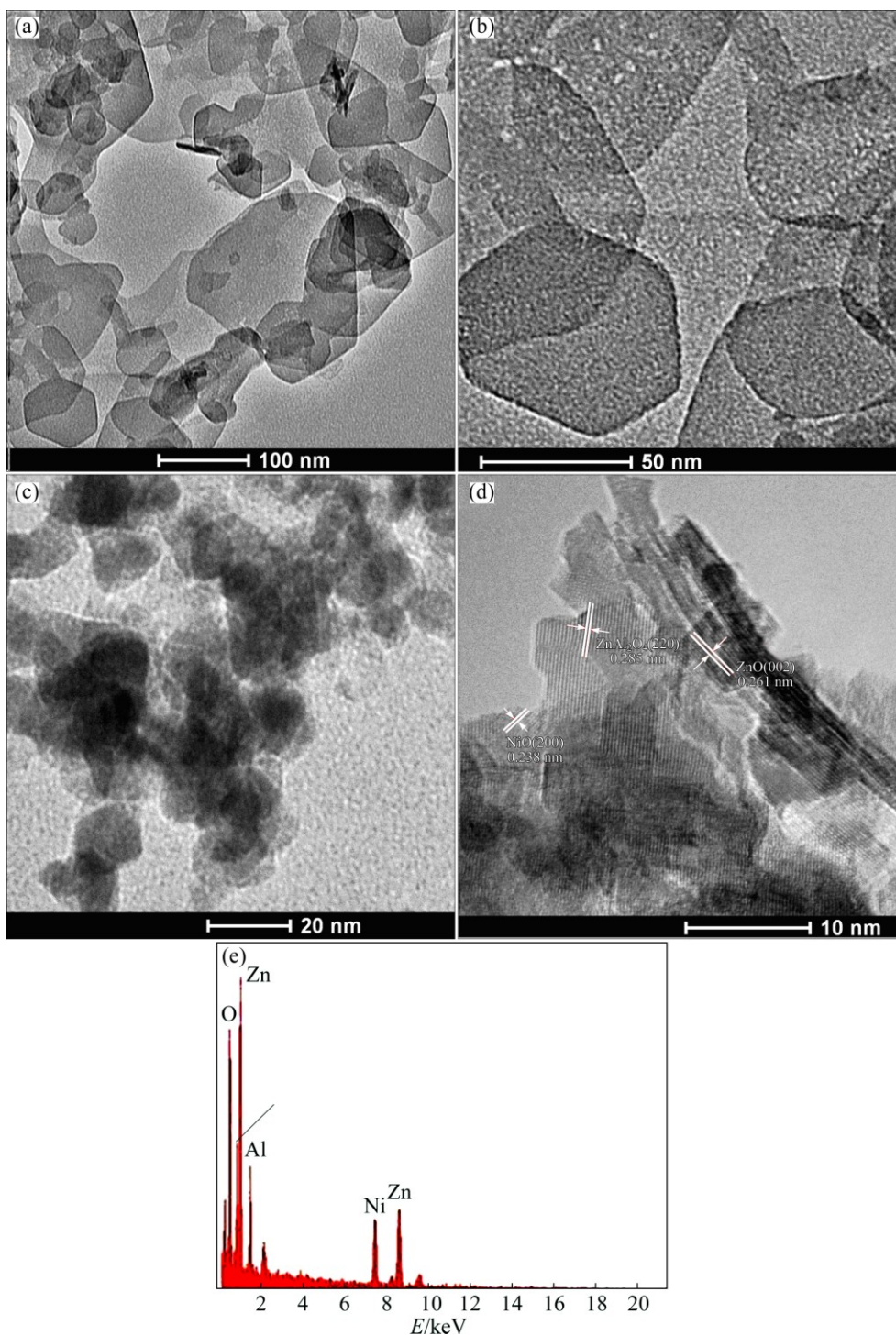


Fig. 6 TEM and HRTEM images of ZNA-2-LDH (a, b) and ZNA-2-500 (c, d) along with EDX measurement of ZNA-2-500 (e)

ZnAl₂O₄. There are also well-defined lattice fringes (Fig. 6(d)): the spacing of 0.261 and 0.238 nm can be ascribed to (002) and (200) planes of ZnO and NiO phase, respectively, whereas that of 0.285 nm corresponds to (220) facet of ZnAl₂O₄ phase [8,24]. The uniform lattice fringes provide further evidence in favour of crystalline nature of nanoparticles. The EDX pattern further confirms the presence of Zn, Ni, Al and O elements in ZNA-2-500 (Fig. 6(e)).

Table 1 summarizes the BET surface areas, pore volumes, and average pore sizes of ZNA-2-LDH before and after calcination. It is apparent that the calcination temperature has an influence on the physical properties of the samples. Upon calcination, there is an increase in BET surface area and total pore volume, but a decrease in pore diameter. Such phenomena may be attributed to the destruction of the layered structure, which results in the formation of crystalline oxides phases. Sample I is

the ZNA-2-LDH before calcination. Sample II obtained after calcination at 400 °C shows a larger specific surface area (170.6 m²/g) than Samples III and IV. With increasing calcination temperature to 500 °C (Sample III), the BET specific surface areas decrease from 170.6 to 153.5 m²/g. However, when calcination temperature is further raised to 600 °C, the BET specific surface areas decrease to 144.2 m²/g. The difference may be attributed to the sintering of the oxides and the degree of crystallinity. Nonetheless, the specific surface areas of Samples III and IV are still much higher than that of ZnO/ZnAl₂O₄ reported by ZHAO et al [8].

Table 1 BET and pore-structure data of samples calcined at different temperatures

Sample No.	Calcination temperature/°C	$S_{\text{BET}}/(\text{m}^2 \cdot \text{g}^{-1})$	Average pore diameter/nm	Pore volume/ $(\text{cm}^3 \cdot \text{g}^{-1})$
I	Not calcined	73.8	15.9	0.29
II	400	170.6	8.8	0.37
III	500	153.5	9.9	0.36
IV	600	144.2	7.2	0.28

Figure 7 presents the nitrogen adsorption–desorption isotherms as well as the corresponding pore size distribution curves of ZNA-2-LDH before and after calcination. All the samples exhibit typical IV isotherms (Fig. 7(a)), and each isotherm shows a distinct type-H₃ hysteresis loop characteristic of mesoporous materials [25]. As shown in Fig. 7(b), the pore size distribution plots of the samples are relatively wide, ranging from 2 to 70 nm. The average pore diameters follow the order: not calcined > 500 °C > 400 °C > 600 °C. This difference may be explained by the formation of oxides, which probably results in the collapse of the large pores and decreasing of the average pore diameter. It is also found that ZNA-2-500 has larger pore size distribution (9.9 nm) compared with ZNA-2-400 and ZNA-2-600. Despite ZNA-2-500 has no largest surface areas among the three, it is estimated that its large pores promote the adsorption of dye molecules and desorption of products, leading to better catalytic activity.

The UV–Vis diffuse reflectance spectra of ZNA-2-500 and ZA-3-500 samples are shown in Fig. 8. It is seen that spectral intensity of ZNA-2-500 (Fig. 8(b)) is higher than that of ZA-3-500 (Fig. 8(a)) because of the incorporation of Ni²⁺ cation, which corresponds to ZA-3-500 at ~416 nm and ZNA-2-500 at ~489 nm, respectively. The band gap energies of the two samples were calculated using the onset of the UV–Vis spectra of the absorption values with equation, $E_g = hc/\lambda = 1240/\lambda$ [26]. The average band gap energies for

ZA-3-500 and ZNA-2-500 were thus calculated to be 2.98 and 2.54 eV, respectively. The ZNA-2-500 exhibits lower band gap energy and is expected to show better photocatalytic activity compared with ZA-3-500. This result can be attributed to the coupling interaction among the ZnO, NiO and ZnAl₂O₄ phases, the optimizing content of ZnO, NiO and the form of heterojunction structure, which leads to the enhancement of utilization of light and photocatalytic activity [8].

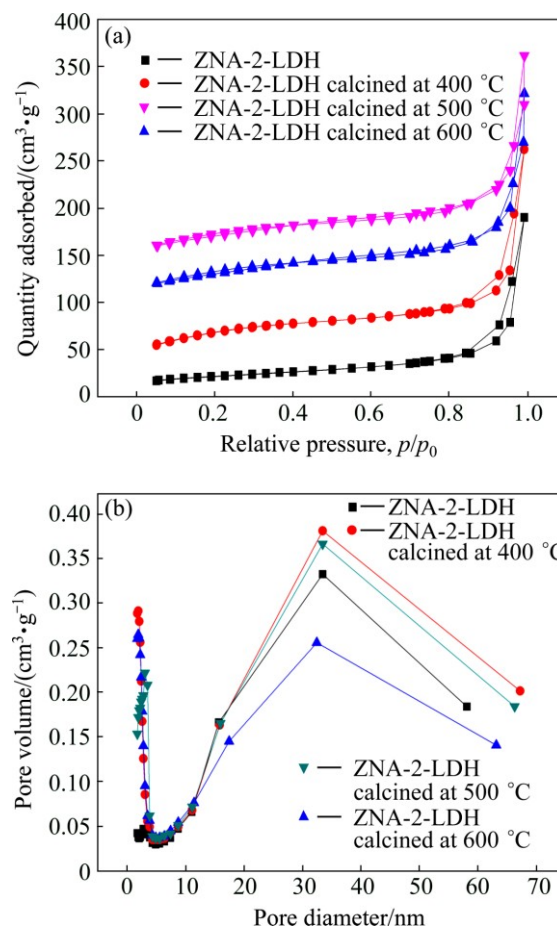


Fig. 7 N₂ adsorption–desorption isotherms (a) and pore size distribution (b) of samples

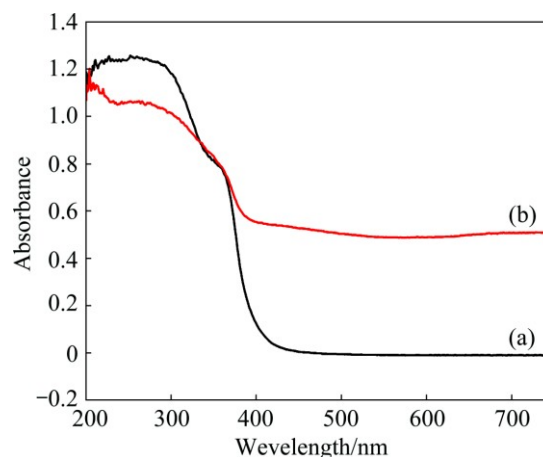


Fig. 8 UV–Vis spectra of ZA-3-500 (a) and ZNA-2-500 (b)

3.2 Photocatalytic activity

Figure 9(a) displays the effect of $\text{Zn}^{2+}/\text{Ni}^{2+}/\text{Al}^{3+}$ composition in the ZNA-2-500 sample on methyl orange (MO) degradation. It can be seen that the content of Zn^{2+} has certain impacts on the decolorization rate. It is found that the ZNA-2-500 shows the best photocatalytic activity among the samples. The highest decolorization rate of MO reaches 97.3% within 60 min under simulated sunlight irradiation. However, the photocatalytic activity decreases with further increasing Zn^{2+} content (ZNA-3-500, decolorization rate of 90.4%). It is more likely caused by the interfacial heterostructure and well-crystalline in ZNA-2-500 (Figs. 2 and 6). Firstly, the effective heterojunction with good transfer channels to separate electrons and holes could be formed at the interface between appropriate amount of ZnO, NiO and ZnAl_2O_4 [8]. The efficient separation of the photogenerated e^- and h^+ pairs is regarded as the key factor for the high photocatalytic activities [27]. Secondly, it has been reported that an insulating layer of oxides (e.g., Al_2O_3 or ZnO) could act as a barrier to effectively inhibit the recombination of charge carriers in semiconductors due to their large band gaps, thus resulting in better photocatalytic activity [28]. However, the excessive ZnO would result in simultaneous suppression of forward and backward transfer of electrons [11]. It seems to be a reasonable interpretation to elucidate why ZNA-3-500 performs more poorly than ZNA-2-500.

The photocatalytic activities of ZNA-2-LDH before and after calcination are shown in Fig. 9(b). As expected, the ZnNiAl-LDH before calcination shows very low photocatalytic activity. The result may well be correlated with XRD observation that only a small amount of $\text{Zn}(\text{OH})_2$ exists at this stage, and the rest of Zn^{2+} and Ni^{2+} ions are incorporated in the brucite-like sheets. Improved photocatalytic activity is observed over the calcined samples. Within 60 min, ZNA-2-400 shows an improved activity (MO decolorization rate of 76.2%), a little higher than that of ZNA-2-600. The improved activity could be partly ascribed to the larger specific surface area of ZNA-2-400 ($170.6 \text{ m}^2/\text{g}$) than that of ZNA-2-600 ($144.2 \text{ m}^2/\text{g}$), and thus stronger adsorption capability for dye. However, ZNA-2-500 sample shows the best photocatalytic activity (MO decolorization rate of 97.3%) among the samples although it has no largest specific surface area. Usually, the activity of catalysts increases with the rise of specific surface areas due to better adsorption capability of dye molecules. However, it is known that good crystallinity is also very important to the activity of the photocatalyst [29]. According to the XRD results (Fig. 2), the ZNA-2-500 photocatalyst shows better crystallinity than ZNA-2-400, resulting in higher photocatalytic performance. The strong dye

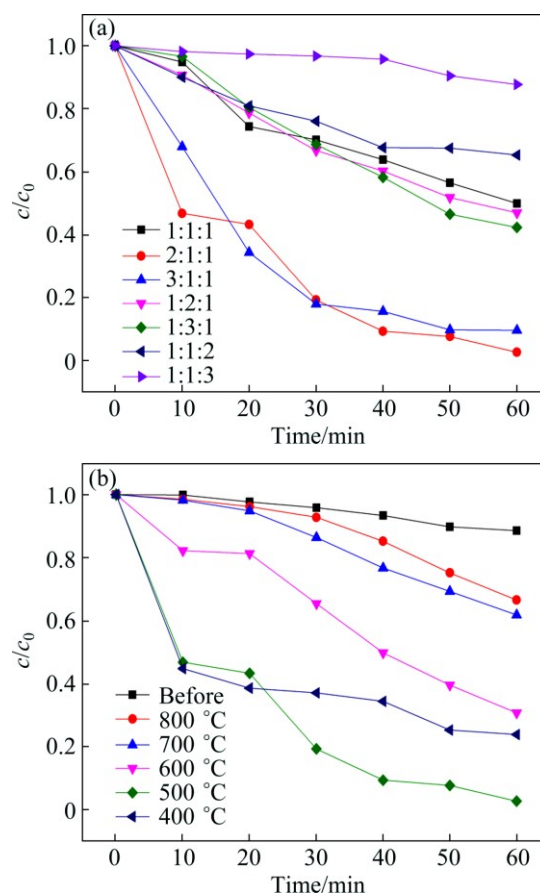


Fig. 9 Effect of Zn/Ni/Al mole ratio (a) and calcination temperature (b) on MO degradation

adsorption in the first 30 min by ZNA-2-500 can be associated with the larger surface area ($153.6 \text{ m}^2/\text{g}$), followed by a gradual decrease of MO concentration due to a photocatalytic reaction. As for ZNA-2-600, the increase of calcination temperature can cause particle size growth and aggregations among the particles, resulting in decrease of photocatalytic activity. Over ZNA-2-700 and ZNA-2-800, there is further decrease in photocatalytic activity (MO decolorization rates of 38.2% and 33.4%, respectively), and such a phenomenon can again be related to the effects of specific surface area and crystallinity.

The comparative results of MO degradation over Degussa P25 TiO_2 , ZA-3-500, and ZNA-2-500 are shown in Fig. 10. Light irradiation in the absence of photocatalyst almost shows no decolorization of MO, suggesting that the photolysis of MO can be ignored. Under dark conditions, the concentration of MO changes obviously in the presence of ZNA-2-500. Since the adsorption capacity of MO on ZNA-2-500 is around 46.2%, this suggests that the MO degradation is dominated by photocatalytic effects. It is obvious that both ZA-3-500 (89.9%) and ZNA-2-500 (97.3%) show better photocatalytic performance than the commercial

P25 TiO₂ (30%), plausibly due to the limited photo responding range of P25 TiO₂. Since ZNA-2-500 performs better than ZA-3-500, it is deduced that the inclusion of Ni²⁺ in the ZnAl-LDH precursor increases the capability for the degradation of MO, in agreement with the observations of LIN et al [30], and the presence of NiO is beneficial for photocatalytic activity [31].

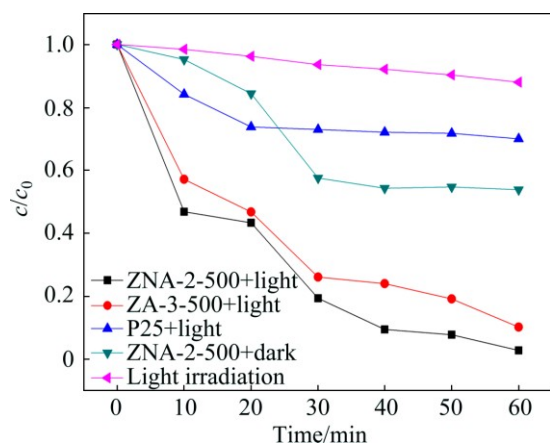


Fig. 10 Comparison of MO degradation over Degussa P25 TiO₂, ZA-3-500, ZNA-2-500 and only light irradiation or catalyst (catalyst, 0.5 g/L; initial MO, 100 mg/L)

As demonstrated in our previous work, the decolorization rate of MO (25 mg/L solution) over the “spheres-in-spheres ZnO/ZnAl₂O₄ composite” (photocatalyst concentration of 0.5 g/L) is 98.7% within 60 min, 8.7% higher than that of Degussa P25 TiO₂ [32]. At such MO concentration, the decolorization rate of MO over ZNA-2-500 is 100% within 10 min under the same conditions. In the present study, we adopted MO concentration of 100 mg/L to study the degradation process. The maximum photocatalytic decolorization rate of 97.3% within 60 min was obtained at ZNA-2-500 concentration of 0.5 g/L (67% higher than that of P25 TiO₂). ZNA-2-500 can be considered as a high-efficient photocatalyst for the degradation of high-concentration MO, and has good prospect in practical treatment of dye-contaminated wastewater.

It is well-known that the radicals (e.g., O₂^{-•}, h⁺, OH[•]) are generated during the irradiation and responsible for the dye degradation [33]. The radical O₂^{-•} is generated via the reduction of adsorbed O₂ on the surface of catalysts by photo-excited electrons and is mostly responsible for dye degradation [11]. The overall photocatalytic process may be shown in Fig. 11. Since the measured band gaps of ZnAl₂O₄ and NiO are relatively high (3.8 and 3.5 eV, respectively), the formation of electron–hole (e⁻/h⁺) pairs due to absorption of sunlight by semiconductor is not easy in the present case, light absorption in the present case mainly occurs by the dye molecule [34] adsorbed on the catalyst surface

and transfers the excited electron into ZnAl₂O₄ and NiO conduction band. The electrons are transferred into CB of ZnO through the heterojunctions as ZnO has a less negative CB potential (−0.31 V (vs NHE)) [35]. The heterostructures of ZnO/ NiO/ZnAl₂O₄ could promote efficient electron transfer via the interfaces. The electrons are scavenged by molecular oxygen (O₂) adsorbed on the surface to form O₂^{-•} radicals, which are dominant species to oxidize the dye [36].

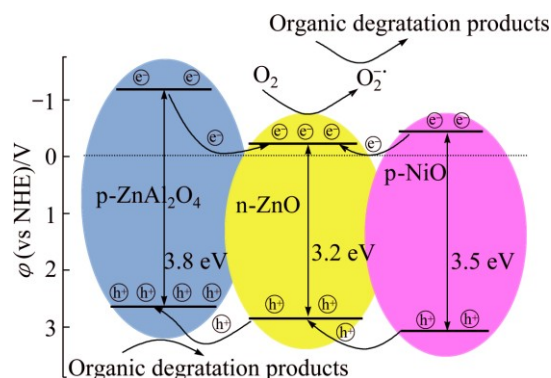


Fig. 11 Mechanism scheme for dye degradation by ZNA-2-500 photocatalyst

4 Conclusions

1) ZnO/NiO/ZnAl₂O₄ mixed-metal oxides with heterojunction structure and high BET surface area were successfully synthesized through a hydrotalcite-like precursor route.

2) The mixed-metal oxide showed superior photocatalytic performance for the degradation of high-concentration MO (100 mg/L). A maximum of 97.3% photocatalytic decoloration rate within 60 min was achieved from the LDH with Zn/Ni/Al mole ratio of 2:1:1 and the calcination temperature of 500 °C.

3) The incorporation of Ni²⁺ cation into ZnAl-LDH enhanced photocatalytic performance for degradation of MO. The synthesis strategy may provide new design and controlled composite materials for environmental purification.

References

- [1] SHI H X, CHEN J Y, LI G Y, NIE X, ZHAO H J, WONG P K, AN T C. Synthesis and characterization of novel plasmonic Ag/AgX–CNTs (X=Cl, Br, I) nanocomposite photocatalysts and synergetic degradation of organic pollutant under visible light [J]. ACS Applied Materials & Interfaces, 2013, 5: 6959–6967.
- [2] HU C, PENG T W, HU X X, NIE Y L, ZHOU X F, QU J H. Plasmon-induced photodegradation of toxic pollutants with Ag–AgI/Al₂O₃ under visible-light irradiation [J]. Journal of the American Chemical Society, 2010, 132: 857–862.
- [3] PARIDA K, MOHAPATRA L, BALIARSINGH N. Effect of Co²⁺ substitution in the framework of carbonate intercalated Cu/Cr LDH

- on structural, electronic, optical, and photocatalytic properties [J]. *Journal of Physical Chemistry C*, 2012, 113: 22417–22424.
- [4] BALLARSINGH N, MOHAPATRA L, PARIDA K. Design and development of a visible light harvesting Ni–Zn/Cr–CO₃²⁻ LDH system for hydrogen evolution [J]. *Journal of Materials Chemistry A*, 2013, 1: 4236–4243.
- [5] PARADA K, SATPATHY M, MOHAPATRA L. Incorporation of Fe³⁺ into Mg/Al layered double hydroxide framework: effects on textural properties and photocatalytic activity for H₂ generation [J]. *Journal of Materials Chemistry*, 2012, 22: 7350–7357.
- [6] CHEN G X, QIAN S M, TU X M, WEI X Y, ZOU J P, LENG L H, LUO S L. Enhancement photocatalytic degradation of rhodamine B on nano Pt intercalated Zn–Ti layered double hydroxides [J]. *Applied Surface Science*, 2014, 293: 345–351.
- [7] del MARTIN CAMPO E, VALENTE J S, PAVON T, ROMERO R, MANTILLA A, NATIVIDAD R. 4-chlorophenol oxidation photocatalyzed by a calcined Mg–Al–Zn layered double hydroxide in a co-current downflow bubble column [J]. *Industrial & Engineering Chemistry Research*, 2011, 50: 11544–11552.
- [8] ZHAO X F, WANG L, XU X, LEI X D, XU S L, ZHANG F Z. Fabrication and photocatalytic properties of novel ZnO/ZnAl₂O₄ nanocomposite with ZnAl₂O₄ dispersed inside ZnO network [J]. *AIChE Journal*, 2012, 58: 573–582.
- [9] CARRIAZO D, del ARCO M, GARCIA-LOPEZ E, MARCI G, MARTIN C, PALMISANO L, RIVES V. Zn, Al hydrotalcites calcined at different temperatures: Preparation, characterization and photocatalytic activity in gas-solid regime [J]. *Journal of Molecular Catalysis A (Chemical)*, 2011, 83–90: 342–343.
- [10] LAN M, FAN G L, SUN W, LI F. Synthesis of hybrid Zn–Al–In mixed metal oxides/carbon nanotubes composite and enhanced visible–light-induced photocatalytic performance [J]. *Applied Surface Science*, 2013, 282: 937–946.
- [11] XIANG X, XIE L S, LI Z W, LI F. Ternary MgO/ZnO/In₂O₃ heterostructured photocatalysts derived from a layered precursor and visible–light-induced photocatalytic activity [J]. *Chemical Engineering Journal*, 2013, 221: 222–229.
- [12] SEFTEL E M, PUSCASU M C, MERTENS M, COOL P, CARJA G. Assemblies of nanoparticles of CeO₂–Zn–Ti–LDHs and their derived mixed oxides as novel photocatalytic systems for phenol degradation [J]. *Applied Catalysis B (Environmental)*, 2014, 150–151: 157–166.
- [13] DUTTA K, DAS S, PRAMANIK A. Concomitant synthesis of highly crystalline Zn–Al layered double hydroxide and ZnO: Phase interconversion and enhanced photocatalytic activity [J]. *Journal of Colloid and Interface Science*, 2012, 366: 28–36.
- [14] SHAO M F, HAN J B, WEI M, EVANS D G, DUAN X. The synthesis of hierarchical Zn–Ti layered double hydroxide for efficient visible-light photocatalysis [J]. *Chemical Engineering Journal*, 2011, 168: 519–524.
- [15] SAHU R K, MOHANTA B S, DAS N N. Synthesis, characterization and photocatalytic activity of mixed oxides derived from ZnAlTi ternary layered double hydroxides [J]. *Journal of Physics and Chemistry of Solids*, 2013, 74: 1263–1270.
- [16] EVANS D G, SLADE R C T. *Structural aspects of layered double hydroxides* [M]. Beilin: Springer-Verlay, 2006: 1–87.
- [17] SUN Y Q, ZHOU Y M, WANG Z Q, YE X Y. Structural and morphological transformations of Zn–Al layered double hydroxides through hydrothermal treatment [J]. *Applied Surface Science*, 2009, 255: 6372–6377.
- [18] AHMED A A A, TALIB Z A, BIN HUSSEIN M Z, ZAKARIA A. Improvement of the crystallinity and photocatalytic property of zinc oxide as calcination product of Zn–Al layered double hydroxide [J]. *Journal of Alloys and Compounds*, 2012, 539: 154–160.
- [19] ZOU L, LI F, XIANG X, EVANS D G, DUAN X. Self-generated template pathway to high-surface-area zinc aluminate spinel with mesopore network from a single-source inorganic precursor [J]. *Chemistry of Materials*, 2006, 18: 5852–5859.
- [20] ZHAO X F, ZHANG F Z, XU S L, EVANS D G, DUAN X. From layered double hydroxides to ZnO-based mixed metal oxides by thermal decomposition: Transformation mechanism and UV-blocking properties of the product [J]. *Chemistry of Materials*, 2010, 22: 3933–3942.
- [21] DAS N N, KONAR J, MOHANTA M K, SRIVASTAVA S C. Adsorption of Cr(VI) and Se(IV) from their aqueous solutions onto Zr⁴⁺-substituted ZnAl/MgAl-layered double hydroxides: Effect of Zr⁴⁺ substitution in the layer [J]. *Journal of Colloid and Interface Science*, 2004, 270: 1–8.
- [22] VELU S, RAMASWAMY V, SIVASANKER S. New hydrotalcite-like anionic clays containing Zr⁴⁺ in the layers [J]. *Chemical Communications*, 1997, 21: 2107–2108.
- [23] KOILRAJ P, KANNAN S. Phosphate uptake behavior of ZnAlZr ternary layered double hydroxides through surface precipitation [J]. *Journal of Colloid and Interface Science*, 2010, 341: 289–297.
- [24] ZHANG L, YAN J H, ZHOU M J, YU Y P, LIU Y, LIU Y N. Photocatalytic degradation and inactivation of *Escherichia coli* by ZnO/ZnAl₂O₄ with heteronanostructures [J]. *Transactions of Nonferrous Metals Society of China*, 2014, 24(3): 743–749.
- [25] SING K, EVERETT D, HAUL R, MOSCOU L, PIEROTTI R, ROUQUEROL J, SIEMIENIEWSKA T. Reporting physisorption data for gas/solid systems with special reference to the determination of surface area and porosity [J]. *Pure and Applied Chemistry*, 1985, 57: 603–619.
- [26] HUSSAIN M, RUSSO N, SARACCO G. Photocatalytic abatement of VOCs by novel optimized TiO₂ nanoparticles [J]. *Chemical Engineering Journal*, 2011, 166: 138–149.
- [27] LIANG J, ZHANG C X, DONG H L, HE X, SHEN Y Q, XU B S. Ag/ZnO/ZnSe heteronanostructure: Synthesis and photocatalytic properties with visible light irradiation [J]. *Chinese Journal of Inorganic Chemistry*, 2015, 31(2): 260–266. (in Chinese)
- [28] KIM W, TACHIKAWA T, MAJIMA T, CHOI W Y. Photocatalysis of dye-sensitized TiO₂ nanoparticles with thin overcoat of Al₂O₃: Enhanced activity for H₂ production and dechlorination of CCl₄ [J]. *The Journal of Physical Chemistry C*, 2009, 113: 10603–10609.
- [29] LI D, HANEDA H. Morphologies of zinc oxide particles and their effects on photocatalysis [J]. *Chemosphere*, 2003, 51: 129–137.
- [30] LIN H Y, CHEN Y F, CHEN Y W. Water splitting reaction on NiO/InVO₄ under visible light irradiation [J]. *International Journal of Hydrogen Energy*, 2007, 32: 86–92.
- [31] LEE D S, CHEN H J, CHEN Y W. Photocatalytic reduction of carbon dioxide with water using InNbO₄ catalyst with NiO and Co₃O₄ cocatalysts [J]. *Journal of Physics and Chemistry of Solids*, 2012, 73: 661–669.
- [32] ZHANG L, YAN J H, ZHOU M J, YANG Y H, LIU Y N. Fabrication and photocatalytic properties of spheres-in-spheres ZnO/ ZnAl₂O₄ composite hollow microspheres [J]. *Journal of Applied Surface Science*, 2013, 268: 237–245.
- [33] WU S S, JIA Q M, SUN Y L, SHAN S Y, JIANG L H, WANG Y M. Microwave-hydrothermal preparation of flower-like ZnO microstructure and its photocatalytic activity [J]. *Transactions of Nonferrous Metals Society of China*, 2012, 22: 2465–2470.
- [34] RAJESHWAR K, OSUGI M E, CHANMANEE W, CHENTHAMARAKSHAN C R, ZANONI W V B, KAJITVICHYANUKUI P, KRISHNAN-AYER R. Heterogeneous

- photocatalytic treatment of organic dyes in air and aqueous media [J]. Journal of Photochemistry and Photobiology C: Photochemistry Reviews, 2008, 9: 171–192.
- [35] WEI S Q, CHEN Y Y, MA Y Y, SHAO Z C. Fabrication of CuO/ZnO composite films with cathodic co-electrodeposition and their photocatalytic performance [J]. Journal of Molecular Catalysis A: Chemical, 2010, 331: 112–116.
- [36] XU X, LU R J, ZHAO X F, XU S L, LEI X D, ZHANG F Z, EVANS D G. Fabrication and photocatalytic performance of a $Zn_xCd_{1-x}S$ solid solution prepared by sulfuration of a single layered double hydroxide precursor [J]. Applied Catalysis B (Environmental), 2011, 102: 147–156.

ZnNiAl 水滑石基复合金属氧化物的 制备及其高效光催化性能

张丽¹, 戴超华¹, 张秀秀³, 刘又年², 阎建辉^{1,2,3}

1. 湖南理工学院 化学化工学院, 岳阳 414006;
2. 中南大学 化学化工学院, 长沙 410083;
3. 湘潭大学 化工学院, 湘潭 411105

摘要: 采用水热法将 ZnNiAl 金属盐溶液混合制得一系列水滑石前驱体, 通过在不同温度下焙烧后获得 ZnO/NiO/ZnAl₂O₄ 纳米复合物。利用 SEM、HRTEM、TEM、XRD、BET、TG-DTA 和 UV-Vis DRS 测试方法对样品进行表征。在模拟太阳光照射下, 通过测定甲基橙溶液的光催化降解率来评价样品的光催化活性。研究 Zn/Ni/Al 摩尔比、焙烧温度等对样品结构组成、形貌及光催化活性的影响。结果表明, 相比水滑石前驱体, ZnO/NiO/ZnAl₂O₄ 纳米复合物有更好的光催化性能, 当原料中 Zn/Ni/Al 摩尔比为 2:1:1 时, 在 600 °C 焙烧所得的催化剂具有最佳光催化活性。在模拟太阳光照射下, 60 min 内对浓度为 100 mg/L 甲基橙的降解率达 97.3%, 相同条件下远远超过了 Degussa P25 的活性。并且对 ZnO/NiO/ZnAl₂O₄ 纳米复合物可能的光催化机理进行了探讨。

关键词: ZnNiAl 水滑石; 复合金属氧化物; 光催化降解; 光催化性能

(Edited by Wei-ping CHEN)